

# Motion-compensated cardiac MRI using low-rank diffeomorphic flow (DMoCo)

Joseph William Kettelkamp, Ludovica Romanin, PhD, Sarv Priya, MD, and Mathews Jacob, PhD,

**Abstract**—We introduce an unsupervised motion-compensated image reconstruction algorithm for free-breathing and ungated 3D cardiac magnetic resonance imaging (MRI). We express the image volume corresponding to each specific motion phase as the deformation of a single static image template. The main contribution of the work is the low-rank model for the compact joint representation of the family of diffeomorphisms, parameterized by the motion phases. The diffeomorphism at a specific motion phase is obtained by integrating a parametric velocity field along a path connecting the reference template phase to the motion phase. The velocity field at different phases is represented using a low-rank model. The static template and the low-rank motion model parameters are learned directly from the k-space data in an unsupervised fashion. The more constrained motion model is observed to offer improved recovery compared to current motion-resolved and motion-compensated algorithms for free-breathing 3D cine MRI.

**Index Terms**—diffeomorphism, low-rank, motion compensation, unsupervised, moco

## I. INTRODUCTION

**M**agnetic Resonance (MR) is the gold standard for evaluating cardiac function. The 2D cardiac cine acquisition strategy requires extensive preparatory scans for slice localization and requires breath hold, which many subject groups (e.g., children or patients with reduced tidal volume) cannot comply with. 3D free-breathing and ungated acquisition schemes that offer isotropic spatial resolution and eliminate the need for preparatory scans were recently introduced [2], [9], [10], [12], [15], [17], [18], [23], [26], [27], [29]. These schemes estimate the respiratory and cardiac phases from k-space center, dedicated k-space navigators, or ECG signals. The k-space data is grouped into cardiac and respiratory bins using the above phase information, followed by the joint reconstruction of the images using total variation or low-rank penalties. Although these motion-resolved approaches offer great promise, the main challenge is the associated long acquisition times to ensure good sampling of the bins. Although supervised deep learning (DL) approaches may offer improved trade-offs, the challenge is the lack of training data; unlike 2D settings, the acquisition of fully sampled images is not possible in our 5D setting. In addition, the extension of current DL methods is challenging because of the enormous memory demand. Recently, patient-specific self-supervised

deep learning methods were introduced [13], [16], [28], [30], [32], [33] to further reduce data demand in motion-resolved 4D (2D+cardiac and respiratory dimensions) MRI. These methods express the image at a specific cardiac and respiratory phase as a nonlinear function of the low-dimensional signals (e.g. cardiac and respiratory motion). In our 5D setting, a large 3D CNN is needed to represent the image volumes in each phase; training of this model using backpropagation will be associated with high memory demand.

Motion-compensated (MoCo) reconstruction schemes that explicitly model the deformations between the phases are significantly more data efficient than the above motion resolved strategies [19], [21], [24], [31]. Because they combine the information from the different bins, they are less sensitive to varying numbers of samples in each bin. The main drawback of these methods is the high computational complexity of image registration. Deep learning (DL) methods to estimate respiratory motion [19] and unrolled DL methods that incorporate motion compensation have been recently introduced [22]. These methods are not directly applicable to our 5D setting due to the extreme undersampling of the bins, the high memory demand, and the need for fully-sampled reference data. An unsupervised DL approach termed MoCo-SToRM [34] was recently introduced for respiratory motion-compensated lung MRI. MoCo-SToRM models the volume in each respiratory phase as the deformed version of a static image template. The motion field at each phase is modeled as the output of a CNN in response to low-dimensional latent vectors that correspond to the phase. The latent vectors, the CNN parameters, and the image template are jointly estimated from the undersampled k-t space data of each subject, similar to self-supervised motion-resolved strategies [13], [16], [28], [30], [32], [33].

We introduce an unsupervised approach for the recovery of motion-compensated cardiac cine acquired using free breathing and ungated 3D-SSFP acquisitions. Similar to MoCo-SToRM [14], we represent the image in each phase (cardiac and respiratory) as the deformed version of a static image template. The main distinction of the proposed scheme is the more constrained low-rank diffeomorphic motion model. The deformation model in MoCo-SToRM does not guarantee that the deformation of the heart and surrounding tissues maintains integrity and connectivity, preventing any inter-sections between different regions. The lack of regularity constraints translates to inaccurate motion estimates when the phases are heavily undersampled (e.g. around 100x or more). We are motivated by diffeomorphic models used in medical image registration that represents the deformation between two images as an invertible function, such that both the function

This work is supported by NIH grants: R01EB019961, R01AG067078, and R01AG087159. Joseph William Kettelkamp and Mathews Jacob are with University of Virginia (e-mail:trz8sp,mjacob@virginia.edu). Ludovica Romanin is with Siemens Healthineers International AG, Lausanne, Switzerland. Sarv Priya is with University of Wisconsin in Madison. The clinical data was acquired at the University of Iowa Hospitals and Clinics (UIHC).

and its inverse are continuously differentiable [3], [8], i.e., smooth. These schemes express the deformation as the time integral of a time-varying vector field, which guarantees the above properties.

The main contribution of this work is the low-rank model for the compact joint representation of the family of diffeomorphisms. This is a generalization of current diffeomorphic models, which consider the registration of a pair of images, to the joint registration of a family of images. In particular, we model the deformation at each motion phase as the integral of a phase-dependent velocity field along a linear path connecting the template phase and the desired phase. We note that the collection of the velocity fields at different motion phases is significantly more low-rank than the original images and even the deformation fields at different phases; the low-rank velocity model thus offers a compact representation of the diffeomorphisms and hence the images. We additionally incorporate regularization prior to encourage the diffeomorphisms to be independent of the integration path, which further reduces the degree of freedom. We estimate the velocity fields and the static template from the measured k-space data in an unsupervised fashion. The coupling of the motion fields at different phases via the overlapping path integrals, the use of velocity constraints to make the path of the deformations independent, and the low-rank model make the deformation model more constrained than the unsupervised approach in [34] and the supervised approach [19]. This enables us to extend the MoCo approach to the cardiac and respiratory resolved recovery from six minutes of acquisition. This work builds on our previous conference paper [14], which used the MoCo-SToRM [34] motion model for 5D cardiac MRI.

## II. BACKGROUND

### A. Multichannel MRI Acquisition

The multichannel acquisition of the data can be mathematically modeled as:

$$\mathbf{b}(t) = \mathcal{A}_{\mathbf{k}(t)}(\rho_t(\mathbf{r})) + \mathbf{n}(t). \quad (1)$$

Here,  $\mathbf{r} = (x, y, z) \in \mathbb{R}^3$  denotes the spatial variable and  $t$  denotes the time at which the k-space measurements  $\mathbf{b}(t)$  were acquired.  $\rho_t$  denotes the spatial volume at time instant  $t$  and  $\mathcal{A}_{\mathbf{k}(t)}$  denotes the multichannel Fourier transform corresponding to the k-space locations  $\mathbf{k}(t)$ .  $\mathbf{n}(t)$  denotes the measurement noise of variance  $\sigma^2$ .

### B. Diffeomorphic Image Registration

Given two  $n$ -dimensional image volumes  $I_0, I_1 \in \mathbb{R}^n \rightarrow \mathbb{C}$ , image registration aims to find a deformation  $\phi_1 : \mathbb{R}^n \rightarrow \mathbb{R}^n$  such that  $I_1(\mathbf{r}) = I_0(\phi_1(\mathbf{r}))$ . A deformation may be evaluated as  $\phi_1(\mathbf{r}) = \mathbf{r} + \mathbf{u}(\mathbf{r})$ , where  $\mathbf{u}$  denotes the displacement. Although its inverse may be approximated as  $\mathbf{r} = \phi_1(\mathbf{r}) - \mathbf{u}(\phi_1(\mathbf{r}))$ , this is only as exact when  $\mathbf{u}(\mathbf{r}) \rightarrow \mathbf{u}(\phi(\mathbf{r}))$ ; that is, for small deformations that satisfy  $\mathbf{u} \rightarrow 0$ . One can compose several infinitesimal deformations

$$\phi_N(\mathbf{r}) = (\mathbf{r} + \mathbf{u}_N(\mathbf{r})) \circ \dots \circ (\mathbf{r} + \mathbf{u}_0(\mathbf{r})),$$

to obtain a large deformation that is invertible. This intuition has led to the representation of diffeomorphisms, which are often expressed as an endpoint of a flow.  $\phi_\delta(\mathbf{r}) : [0, 1] \times \mathbb{R}^n \rightarrow \mathbb{R}^n$ , associated with a smooth  $n$ -dimensional vector field  $\nu_\delta(\mathbf{r}) : [0, 1] \times \mathbb{R}^n \rightarrow \mathbb{R}^n$ , specified by the ordinary differential equation [6], [8]

$$\frac{d\phi_\delta(\mathbf{r})}{d\delta} = \nu_\delta(\phi_\delta(\mathbf{r})); \quad \phi_0(\mathbf{r}) = \mathbf{r}.$$

The above ODE is solved as

$$\phi_1(\mathbf{r}) = \underbrace{\phi_0(\mathbf{r})}_{\mathbf{r}} + \int_0^1 \nu_\delta(\phi_\delta(\mathbf{r})) d\delta \quad (2)$$

(2) can be inverted by running the ODE backwards with an initialization  $\phi_1(\mathbf{r}) = \mathbf{r}$  as

$$\mathbf{r} = \phi_1(\mathbf{r}) + \int_1^0 \nu_\delta(\phi_\delta(\mathbf{r})) d\delta \quad (3)$$

## III. LOW-RANK DFFEOMORPHIC IMAGE MODEL

Unlike motion-resolved methods that group the readouts into discrete bins and jointly recover the binned images, we represent the image volume  $\rho_t(\mathbf{r})$  at the time instant  $t$  as the function of the continuous phase variable  $\tau(t) \in \mathbb{R}^2$ .

$$\tau(t) = \begin{bmatrix} c(t) \\ r(t) \end{bmatrix} \quad (4)$$

Here,  $c(t)$  and  $r(t)$  denote the cardiac and respiratory phase at  $t$ . We assume that the images in the time series depend on the motion phase  $\tau(t)$ . We represent the image volume at time  $t$  specified by  $\rho_t(\mathbf{r})$  at the motion phase  $\tau(t)$  as the deformed version of a static template  $\eta : \mathbb{R}^3 \rightarrow \mathbb{C}$ :

$$\rho_t(\mathbf{r}) = \eta(\varphi_{\tau(t)}(\mathbf{r})). \quad (5)$$

Here,  $\varphi_\tau(\mathbf{r})$  is the deformation at the motion phase  $\tau$ .

### A. Parametric Diffeomorphic Motion Model

Most diffeomorphic registration methods consider the registration of a pair of images. In this work, we consider the joint registration of images  $\rho_t(\mathbf{r})$  using a parametric family of diffeomorphisms, parameterized by  $\tau$ . The diffeomorphisms are represented in terms of a parametric velocity tensor  $\mathbf{v}_\tau\left(\frac{d\tau}{dt}, \mathbf{r}\right)$  at the motion phase  $\tau$ . The tensor  $\mathbf{v}_\tau$  can be thought of as the concatenation of two velocity fields. For instance, the first component of the tensor denoted by  $\mathbf{v}_\tau(0, \mathbf{r})$  is the tissue velocity at the phase  $\tau$ , when the cardiac phase increases at the rate  $dc/dt = 1$ . When both phases are increased at a speed  $\tau' = [dc/dt \quad dr/dt]^T$ , we assume linearity and obtain the tissue velocity as

$$\mathbf{v}_\gamma(0, \mathbf{r}) \frac{dc}{dt} + \mathbf{v}_\gamma(1, \mathbf{r}) \frac{dr}{dt} = \left\langle \mathbf{v}_\gamma(\mathbf{r}), \frac{d\tau}{dt} \right\rangle.$$

We now consider a curve  $\gamma : [0, 1] \rightarrow \mathcal{C}_\tau$  in phase space (see Fig. 1) starting at  $\mathbf{0}$  and ending at  $\tau$  with  $\gamma(0) = \mathbf{0}$  and  $\gamma(1) = \tau$  to define the diffeomorphism  $\varphi_\tau(\mathbf{r})$ . Here,  $\gamma(\delta)$  are

points on the curve and  $\delta$  is an arbitrary parameterization. For the curve  $\mathcal{C}_\tau$ , we consider the one-parameter velocity field:

$$\mathbf{v}_\delta(\mathbf{r}) = \left\langle \mathbf{v}_{\gamma(\delta)}(\mathbf{r}), \gamma'(\delta) \right\rangle. \quad (6)$$

With this choice and setting  $\phi_0(\mathbf{r}) = \mathbf{r}$ , we obtain the deformation at the phase  $\tau$  as:

$$\varphi_\tau(\mathbf{r}) = \mathbf{r} + \int_0^1 \left\langle \mathbf{v}_{\gamma(\delta)}(\phi_\delta(\mathbf{r})), \gamma'(\delta) \right\rangle d\delta. \quad (7)$$

The above formulation produces parametric deformations  $\varphi_\tau$  that are dependent on the specific curve  $\mathcal{C}_\tau$ . In this work, we define  $\mathcal{C}_\tau$  as a straight line-segment, connecting  $\mathbf{0}$  and  $\tau$ . As discussed in Section II-B, each of the deformation fields  $\varphi_\tau$  can be inverted by running the ODE backwards as in (3). Thus, the image volume at phase  $\tau_1$  can be deformed to phase  $\tau_2$  using the transformation  $\varphi_{\tau_2} \circ \varphi_{\tau_1}^{-1}$ , where  $\circ$  is the composition mapping.

### B. Path constraint on velocity fields

We note that  $\varphi_\tau$  in the previous section depends on the specific choice of the curve  $\mathcal{C}_\tau$ . We now consider a different path  $\beta : [0, 1] \rightarrow \mathcal{D}_\tau$  with  $\mathcal{D}_\tau \neq \mathcal{C}_\tau$  that satisfies  $\beta(0) = \mathbf{0}$  and  $\beta(1) = \tau$ . In this case, we obtain a diffeomorphism:

$$\psi_\tau(\mathbf{r}) = \mathbf{r} + \int_0^1 \left\langle \mathbf{v}_{\beta(\delta)}(\psi_\delta(\mathbf{r})), \beta'(\delta) \right\rangle d\delta \quad (8)$$

With no additional constraints on the velocity field, we may have  $\psi_\tau \neq \varphi_\tau$ . If the integrals were path independent, a diffeomorphism could be directly evaluated from  $\tau_1$  to  $\tau_2$  by integrating the velocity field on a path connecting the two points in phase space rather than evaluating it as  $\varphi_{\tau_2} \circ \varphi_{\tau_1}^{-1}$ .

We note that the constraint  $\psi_\tau = \varphi_\tau$  is not necessary for the representation of the deformations and to realize the algorithm. However, in the interest of reducing the degrees of freedom in the representation, we propose to add a penalty to encourage the diffeomorphisms to be path independent. We consider a penalty involving the path-dependent expected difference in the deformations  $\mathbb{E}_{\mathcal{D}_\tau} \|\psi_\tau - \varphi_\tau\|^2$ . In practice, at each epoch we choose  $\mathcal{D}_\tau$  as a random perturbation of the line segment  $\mathcal{C}_\tau$ . We randomize the perturbations over epochs to ensure that the relation holds for all paths. Our in silico results in Fig. 3 show the benefit of adding this constraint.

### C. Low-rank representation of velocity tensors

The deformations  $\varphi_\tau(\mathbf{r})$  are computed in terms of the velocity fields  $\mathbf{v}_\tau(\mathbf{r})$ , parametrized by phase  $\tau$ . There are extensive similarities between the parametric tissue velocities  $\mathbf{v}_\tau$  at different phases. For example, the deformations in different cardiac phases may be modeled by a relatively constant velocity field, as shown in Fig. 2. In the interest of realizing a compact representation, we propose to use a low-rank model to represent the velocity field:

$$\mathbf{v}_\tau(s, \mathbf{r}) = \sum_{n=0}^R \mathbf{p}_n(\mathbf{r}) m_n(s, \tau) = \mathbf{P}(\mathbf{r}) \mathcal{M}_\kappa(s, \tau) \quad (9)$$

Here  $\mathbf{p}_n(\mathbf{r}) : \mathbb{R}^3 \rightarrow \mathbb{R}^2$  are the spatial basis functions, which are independent of  $s$  and  $\tau$ .  $R$  denotes the rank of

the representation. The weights  $m_k(\tau)$  are nonlinear functions of  $\tau$  and  $s$ . We represent the non-linear function using a multilayer perceptron  $\mathcal{M}_\kappa$  with parameters  $\kappa$ . The unknowns of the deformation model are  $\kappa$ . Because the velocity fields are spatially smooth, we represented  $\mathbf{p}_n(\mathbf{r})$  on a  $32^3$  grid, which is then interpolated to the  $320^3$  volume using trilinear interpolation.

## IV. D-MOCO IMPLEMENTATION

We estimate the static template  $\eta$  and the parameters of the deformation model from the measured k-space data in an unsupervised fashion. We note in (9) that the deformation model  $\varphi_\tau; \forall \tau$  is compactly represented in terms of low-rank factors  $\mathbf{P}$  and MLP weights  $\kappa$ . We introduce the fitting process in Section IV-B, which is also illustrated in Fig. 1. The motion phases are assumed to be predetermined in this step. We derive the cardiac phase  $c(t)$  from the electrocardiogram (ECG). We propose to preestimate the respiratory phase from the superior-inferior (SI) k-space navigators using an autoencoder, as described below.

### A. Pre-estimation of the motion phases

We note that the data are acquired in a free-breathing and ungated fashion. The different readouts  $b(t)$  that are acquired at different time points correspond to different cardiac and respiratory phases. We recorded the ECG triggers, from which we estimated the delay  $c(t)$  of each radial spoke from the previous ECG trigger. We denote the maximum delay as  $C = \max_t c(t)$ .

We propose to estimate the respiratory phase from the SI k-space navigators using an autoencoder. In particular, we reduce the SI signal to a one-dimensional latent variable, which captures the dominant signal variation in the navigator signal that results from respiratory motion. We denote the inverse Fourier transform of multichannel SI k-space navigators, denoted by  $\mathbf{x}(t)$ . We filter  $\mathbf{x}(t)$  with a temporal window of 1 Hz to remove cardiac and other variations in high-frequency signals. We use a fully connected auto-encoder, with a one-dimensional latent vector  $r(t)$ . In particular,  $r(t)$  is the one-dimensional vector that best explains the temporal variations in  $\mathbf{x}(t)$ . The encoder  $\mathcal{E}_{\theta_1}$  is an MLP with two hidden layers with 512 and 256 features, respectively. The decoder  $\mathcal{F}_{\theta_2}$  uses the mirrored architecture, while the weights are not shared between the encoder and the decoder. The auto-encoder parameters are learned such that the loss

$$L(\theta_1, \theta_2) = \sum_t \left\| \mathbf{x}(t) - \mathcal{F}_{\theta_2} \left( \underbrace{\mathcal{E}_{\theta_1}[\mathbf{x}(t)]}_{h(t)} \right) \right\|^2 \quad (10)$$

is minimized.

### B. Self-supervised Loss and Training

The unknowns of the proposed parametric deformable image model are the static template  $\eta$  in (5) and the parameters of the motion model  $\varphi_\tau$ : the spatial basis functions  $\mathbf{P}$  and

MLP parameters  $\kappa$ . We propose to recover these parameters by the minimization of the loss  $L(\eta, \mathbf{P}, \kappa)$ :

$$L = \sum_{\tau} \left( \underbrace{\left\| \mathcal{A}_{\tau}(\eta(\varphi_{\tau}(\mathbf{r}))) - \mathbf{b}_{\tau} \right\|}_{\text{data consistency}}^2 + \underbrace{\lambda_1 \mathbb{E}_{\mathcal{D}_{\tau}} \|\varphi_{\tau} - \psi_{\tau}\|^2}_{\text{velocity constraint}} + \underbrace{\lambda_2 \|\nabla \eta\|^2}_{\text{smoothness penalty}} \right) \quad (11)$$

The first term is the data consistency between the deformed templates and the k-space data. The second term is a penalty to encourage the velocity fields to be path independent as described in Section III-B, and the third is a spatial smoothness penalty on the static template. Here,  $\varphi_{\tau}$  is the deformation obtained by integrating the velocity field along a straight line-segment  $\mathcal{C}_{\tau}$  as in (7).  $\psi_{\tau}$  is the integral along a perturbed path  $\mathcal{D}_{\tau}$  as in (8). The second term involves an expectation over all possible paths between 0 and  $\tau$ . We evaluate both integrals using Euler's summation. The random path is obtained by perturbing the samples on the line by Gaussian noise of variance 10 percent of the step size between the time points. We use different random paths at each iteration of the optimization to encourage the deformation to be independent of the paths.

We minimize the above loss using stochastic gradient descent. At each iteration, we pick a random  $\tau \in [0, 1]^2$ . We choose  $K$  readout groups whose phase is the closest to  $\tau$  in the Euclidean sense to define the loss and hence the gradient. In this work, we chose  $K = 20$ . The hyperparameters are chosen by trial and error on one of the datasets and were kept fixed for the other datasets. We observe that the results were not very sensitive to  $\lambda_1$ , provided that it is large enough to ensure that the deformations are independent of the path. The parameter  $\lambda_2$  was chosen to yield a good compromise between streak artifacts in the reconstructed template  $\eta$  and blurring.

### C. Initialization of motion fields for fast convergence

To speed up the training, we introduce a fast approach to initialize the velocity fields. In particular, we group the k-space readouts to five cardiac and three respiratory motion bins, in an approach similar to XD-GRASP [11]. We reconstructed the images corresponding to each of the bins using a smoothness regularized reconstruction:

$$\rho_{\tau_k} = \arg \min_{\rho} \left\| \mathcal{A}_{\tau_k}(\rho_{\tau_k}) - \mathbf{b}_{\tau_k} \right\|_2^2 + \lambda_3 \|\nabla \rho_{\tau_k}\|_2^2 \quad (12)$$

We note that each of the bins are heavily undersampled. We hence choose a high enough  $\lambda_3$  to obtain a low-resolution reconstruction, free of visible alias artifacts. We set  $\eta = \rho_0$  and solve for  $\tau$  and  $\kappa$  by minimizing the loss:

$$\mathcal{L}_{\text{init}}\{\mathbf{P}, \kappa\} = \sum_k \left\| \eta(\phi_{\tau_k}(\mathbf{r})) - \rho_{\tau_k} \right\|^2 + \lambda_1 \mathbb{E}_{\mathcal{D}_{\tau}} \|\varphi_{\tau} - \psi_{\tau}\|^2 \quad (13)$$

Because this optimization problem does not involve multichannel NUFFT steps, this initialization strategy is computationally

much more efficient than that of (11). We use stochastic gradient descent to derive  $\mathbf{P}$  and  $\kappa_{\text{init}}$ . We note that these parameters are used only to initialize the optimization scheme.

### D. Image Acquisition

The data are acquired using a 3D radial balanced steady-state free precession (bSSFP) research acquisition scheme using a spiral *phyllotaxis* view ordering on a 1.5T MRI scanner (MAGNETOM Aera, Siemens Healthcare, Forchheim, Germany) system using a 32-channel cardiac array. The view order consisted of a superior-inferior (SI) k-space navigator, acquired in every 22 spokes. The temporal resolution of each group of 22 spokes is approximately 70 ms. The number of radial readouts acquired per spoke were 5749, which corresponds to a fixed acquisition time of 5:58 minutes. The main acquisition parameters were: TR/TE of 3.14/1.6 ms, radio frequency excitation angle of  $60^\circ$ , resolution of 1.5 isotropicmm<sup>3</sup>, field of view (FOV) of 240 mm<sup>3</sup>, and readout bandwidth of 840 Hz/pixel [14], [25].

### E. State of the art (SOTA) methods used for comparison

We compare our method against MoCo-SToRM [34]. In MoCo-SToRM, each volume in the time series is modeled as the deformation of a static template, similar to the proposed approach. The main distinction is that the deformation fields are directly represented by a compact model in MoCo-SToRM, unlike the low-rank representation of the velocity fields that are integrated to obtain the deformation fields. To make the comparison fair, we represented the deformations in MoCo-SToRM using a low-rank representation

$$\phi_{\tau}(\mathbf{r}) = \mathbf{Q}(\mathbf{r}) \mathcal{N}_{\kappa}(\tau). \quad (14)$$

similar to (9). Here,  $\mathbf{Q}(\mathbf{r})$  are the  $R$ -dimensional spatial basis vectors and  $\mathcal{N}_{\kappa}$  is an MLP with parameters  $\kappa$ .

We also implemented a motion-resolved (MoR) approach similar to [11]. The cardiac data is binned to three respiratory phases and five cardiac phases [11]. With a short acquisition of 5:58 minutes, it is challenging to resolve more than five cardiac phases. The  $\hat{\rho}_{\tau_{ij}}$  volumes are recovered using (15).

$$\hat{\rho}_{\tau_k} = \arg \min_{\rho} \sum_i \sum_j \left\| \mathcal{A}_{\tau_{ij}}(\rho_{\tau_{ij}}) - \mathbf{b}_{\tau_{ij}} \right\|_2^2 + \lambda_4 \|\nabla \rho\|_1 \quad (15)$$

Here we use the same notation as the above methods. However, we use a temporal regularization between the bins  $\|\nabla_{ij} \rho\|_1$  denotes a total variation penalty. The above motion resolved reconstruction was done using a conjugate gradient algorithm. We also denote the variables as with subscript  $\tau_{ij}$  to show that the reconstruction is discretized to a fixed set of bins.

## V. EXPERIMENTAL SETUP

A challenge in quantitatively validating the proposed approach in an in vivo setting is the lack of fully sampled cardiac and respiratory resolved 3D datasets; the acquisition of these data is impossible. Such data sets are not available to the best of our knowledge. We therefore restrict quantitative

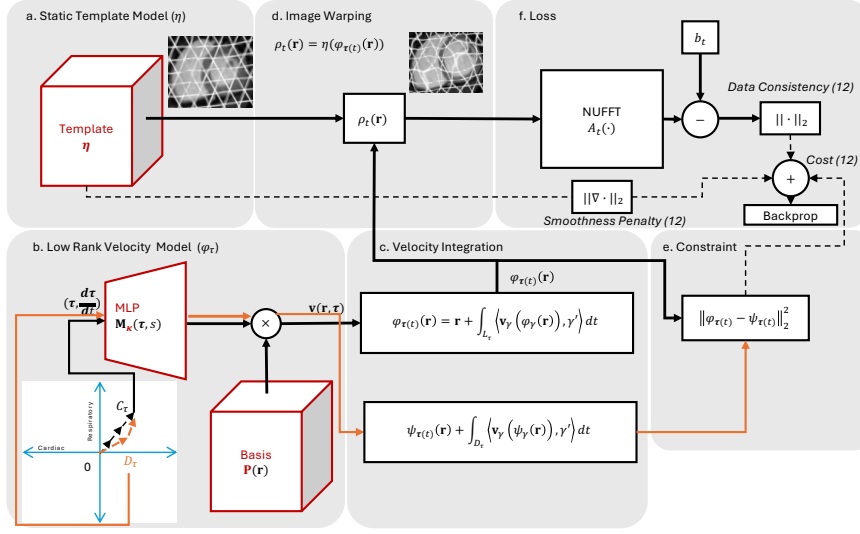


Fig. 1. DMoCo architecture: (a) The static template volume  $\eta$ . (b) The velocity fields at a specific phase  $\tau$  is modeled as the product of the static basis vectors  $\mathbf{P}$  and its weights  $m_{\kappa}(s, \tau)$ . The weights are derived from the cardiac and respiratory phase  $\tau = (c, r)$  using a multilayer perceptron with parameters  $\kappa$ . (c) The deformation field are modeled as a forward diffeomorphic flow, denoted by (7) along the straightline path  $C_{\tau}$ . (d) The static image volume  $\eta$  is interpolated to each phase using trilinear interpolation. (e) The deformation is also derived along an alternate stochastic path  $\mathcal{D}_{\tau}$ ; the difference between the two different deformation estimates at  $\tau$  are used as a penalty, which is the second term in (11). This term ensures that the velocity integrals are path independent, which further constrains the deformation estimates. (f) The forward operator involves multiplication by the coil sensitivity maps and NUFFT. A smoothness penalty is also added to the static template.

comparisons to a numerical phantom generated using XCAT simulations [1] and a 2D annulus with cardiac and respiratory motion Fig. 2. We also compare the proposed method with state-of-the-art methods on in vivo datasets acquired from patients, where we use their breath-held 2D cine acquisitions as reference.

### A. 3D XCAT phantom

An XCAT phantom was used to generate 5749 volumes of repeating respiratory and cardiac patterns. We assumed a respiratory period of 5s and a heart rate of 60 beats per minute. We simulated the k-space measurements by multiplying the phantom by  $B_1$  profile and simulated coil sensitivities of a birdcage coil sensitivity mask with 6 coils and computing the nonuniform fast Fourier transformation of each radial group. Noise of standard deviation  $\sigma = 5 \times 10^{-3}$  was added to the k-space measurements. The image quality metrics were then calculated against the ground truth as well as the respiratory displacements (RD). RD was assessed by measuring the displacement of the left diaphragm dome for the fitted volumes. In addition, we compared the effect of modeling the flow and velocity fields. The total simulated scan time was about six minutes and used the same FOV and resolution as in the *in vivo* study.

### B. 2D Annulus phantom

We use a 2D annulus phantom, considered in Fig. 2, to compare the low-rank approximations of the velocity fields, deformation fields, and the image time series. The 2D setting

makes the computational complexity and memory demand of the low-rank approximations manageable. Here, we consider an annulus that is expanding and contracting to mimic cardiac motion with 60 beats per minute. The cardiac motion was generated using two circles that contract at different rates. The outer circle’s radius decreases by 10% of the FOV while the radius of the inner circle decreases by 14% of the FOV. The phantom also consists of a circular section at the bottom to mimic the liver. We also consider contracting motion with a period of 4s and a displacement of 24%

### C. Human subjects

The in-vivo data was acquired from five cardiac patients at the University of Iowa Hospitals and Clinics (UIHC), according to the institutional review board (IRB) protocols and the consent of the subject. The proposed sequence was added to the end of an existing clinical protocol, approximately 25 to 35 minutes after the short-acting Gadolinium (Gd) contrast agent was administered intravenously.

For qualitative comparisons, we extracted the time series of slices from the 3D reconstructions that closely match the 2D breath-held acquisitions with different views (e.g., short-axis, four-chamber, and two-chamber views). We note that separate breath-holds are required for the acquisition of each of the 2D stacks, while the proposed approach only involves a single free-breathing 3D acquisition. We note that the image contrast of the 3D acquisitions is drastically different from that of the 2D acquisitions, making quantitative image comparisons challenging.

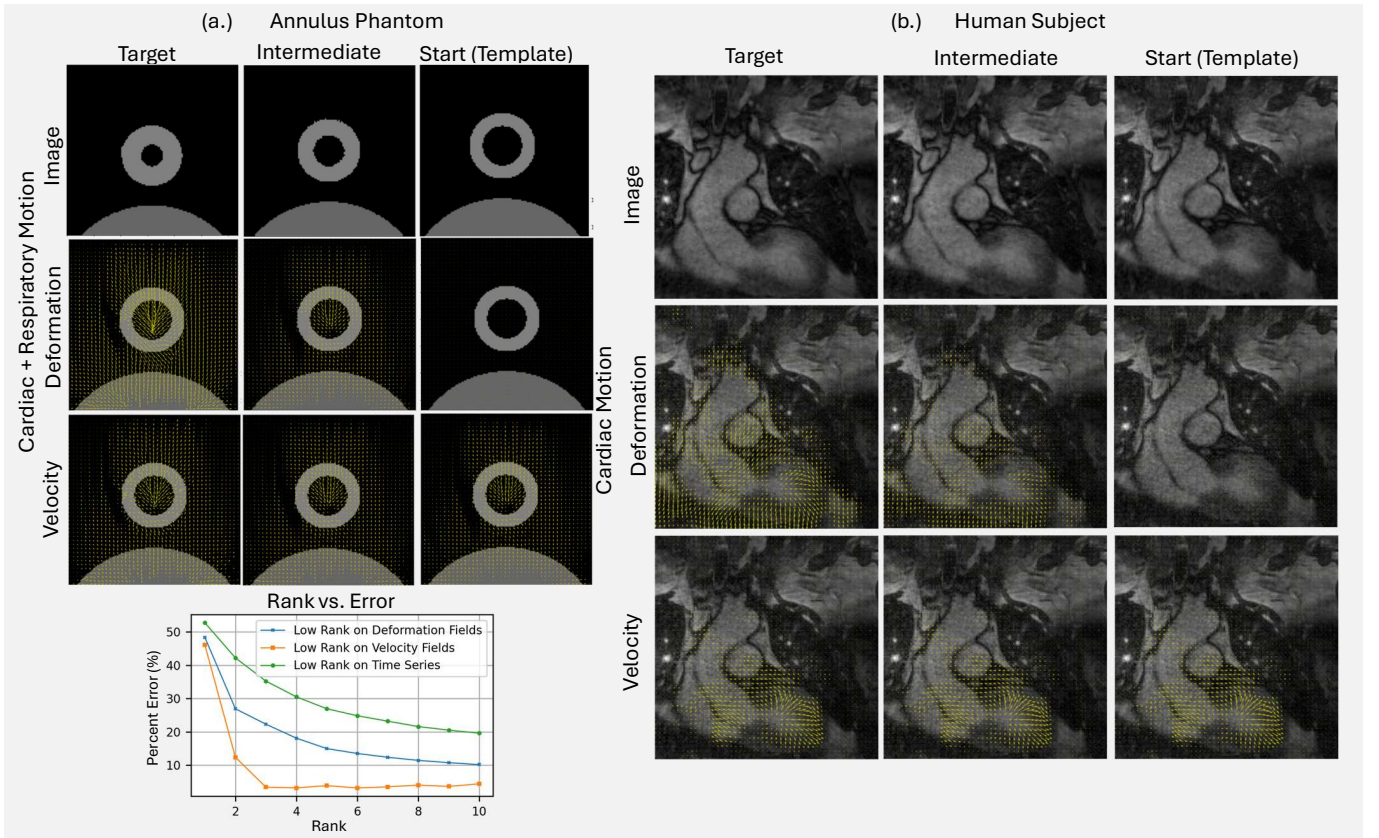


Fig. 2. Low-rank nature of the velocity fields. We show the estimated velocity and deformation maps for a 2D annulus numerical phantom (top-left) and the 3D *in-vivo* dataset (right). The top rows correspond to the images in three different phases, with the right-most image being the template. The middle rows correspond to the estimated deformations, overlaid on the template, while the bottom rows show the velocities in these phases. We note that the velocity fields (bottom rows) are almost the same across different phases, while the corresponding deformations are significantly more complex and changes drastically. In particular, the integration of a relatively static velocity field as in (7) can account for complex time-varying deformation fields. We performed a low-rank approximation of the velocity fields (orange), deformation fields (blue), and the image time series (green) and evaluated the corresponding errors. We observe that a significantly lower rank is sufficient to yield smaller errors, compared to the image time series and even the deformation fields. Here, a rank of 3 on the velocity tensor gave better results than a rank of 10 on the deformation fields. These results show that a deformation model using low-rank modeling of the velocities is very efficient in representing the image time series.

## VI. RESULTS

### A. Impact of low-rank approximation

We first study the low-rank nature of the velocity and deformation tensors in Figure 2 in a 2D annulus phantom in left column (a).

The upper rows show three images at different physiological phases, with the template/source in the systolic phase and the target. The middle image corresponds to an intermediate phase. We perform a joint registration of volumes in the image domain using (13). We overlay the deformation plots on the template in the middle row, while the velocity plots are overlaid in the bottom row. We observe that the velocity fields are roughly similar across all phases, while the deformations are significantly different; the phase-dependent deformations can be obtained by integrating a relatively phase-independent velocity field according to (13). We note that the integration in (6) relies on the velocity fields in the deformed state and therefore are non-linearly dependent on the velocity fields. In

the bottom row 2, we measure the distortion of the deformed images in each phase from the respective reference image as a function of the rank of the velocity (orange), deformation fields (blue), and image series (green). Here, we use a 2D annulus with both respiratory and cardiac motion. We estimated the velocity and the corresponding deformations from the reference images using (13). We then (a) truncated the velocity fields to different ranks, and evaluated the corresponding deformation fields by integrating the approximated velocity fields as in (6), and (b) performed an SVD of the deformation fields at all phases and truncated to a lower rank model. We compare the warped images with the true ones to generate the percent error plots.

The figures show that a rank=3 model on the velocity is sufficient to yield low MSE values 3.45%; converts to 22.3%, while even a rank=10 approximation of the deformation fields can not give the same error rate as a rank=3 model using diffeomorphic flow, 3.45% to 10.2%. The compact velocity representation is expected to yield more robust motion esti-

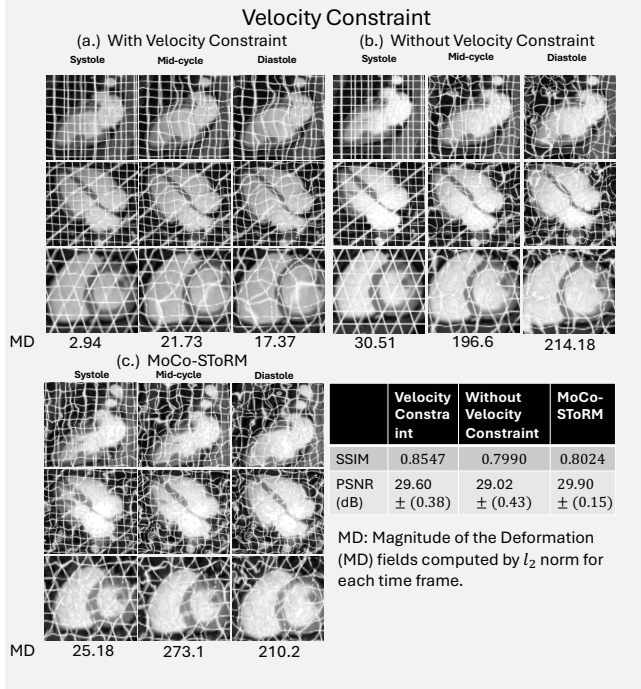


Fig. 3. Impact of the velocity constraint: We show the recovered images and the deformation maps using (a) the proposed model, (b) the proposed model without the velocity constraint, and the MoCo-SToRM method, which directly models the deformation maps rather than integrating the velocities. The  $l_2$  norm of the deformations is reported under each column denoted (MD); a higher number indicates more complex deformation. The results show that the velocity constraint necessarily results in smoother deformations than without it. We also note that the proposed DMoCo model is more constrained than the MoCo-SToRM approach.

mates, especially when estimated from noisy and undersampled images. This is considered in the subsequent experiments.

### B. Impact of velocity constraint

We study the impact of the velocity constraint in (11) in Fig. 3. Here, we used (13) for the joint fit in the image domain, with the end systolic frame as the template. We show the estimated deformations for different cardiac phases, estimated using MoCo-SToRM in (a), the proposed model with the velocity constraint in (b), and without the velocity constraint in (c). We note that all models result in deformed images that closely match the original ones, evidenced by the metrics Fig. 3 table 1. This is expected because noise-free fully sampled images are used for image domain fitting. The results show that without the velocity constraint, the proposed scheme produces highly oscillatory deformations, indicated by the high  $l_2$  norm of the deformation in (c); we note that there are numerous deformations of the template that can yield the targets. The addition of the velocity constraint regularizes the deformations, resulting in deformations with significantly lower  $l_2$  norm in (b). We also note that the deformations offered by MoCo-SToRM in (a), which directly models the deformation fields rather than the velocity fields, result in

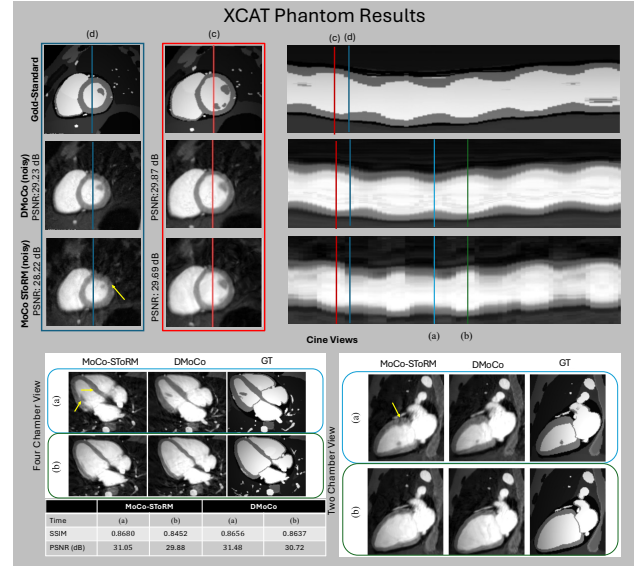


Fig. 4. We used the XCAT framework to simulate a free-breathing and ungated acquisition with the same settings as the in-vivo acquisition. We corrupted the simulated k-space observations with Gaussian noise of standard deviation  $5 \times 10^{-3}$ . We note that the acquisition scheme corresponds to a highly undersampling of several motion phases (e.g., systolic phases in end inspiration). The top three rows show a failure case, where the MoCo-SToRM approach resulted in a discontinuity in the recovered time profiles, shown on the right. This can also be appreciated from the recovered images (left panel with a blue border, corresponding to the blue lines in the time profiles on the right panel) in the corresponding phase, which shows increased blurring and a lower PSNR. By contrast, the DMoCo approach with a more constrained deformation model offers an improved reconstruction of these phases (see yellow arrows). The bottom rows correspond to reconstructions from the systolic and diastolic phases, indicated by the light blue and green lines in the time profile. We observe increased noise blurring in the MoCo-SToRM reconstructions compared to DMoCo.

deformations that are more complex than the proposed scheme. These results show that DMoCo with velocity constraints offer a constrained model that can account for the motion, while yielding smoother deformations. The resulting algorithm is thus expected to be less sensitive to undersampling artifacts and noise, which is studied in the next subsection.

### C. Quantitative comparisons with SOTA methods.

We compare the MoCo-SToRM and DMoCo results on the X-CAT phantom in Fig. 4, where the reconstruction is performed from noisy measurements in k-space. We considered the same sampling pattern as in the in-vivo experiments. We note from the time-profile plots that the MoCo-SToRM results in a piecewise-constant profile with abrupt jumps. We attribute the rapid jumps in the MoCo-SToRM temporal profiles to the less constrained deformation model. By contrast, the DMoCo approach yields smoother profiles, which are consistent with the gold standard. The main distinction between the two approaches is the way in which the deformations are generated. The low rank nature of the velocities that are integrated to obtain the deformations as in (6) and the velocity constraints within DMoCo encourages the deformations to be a smooth

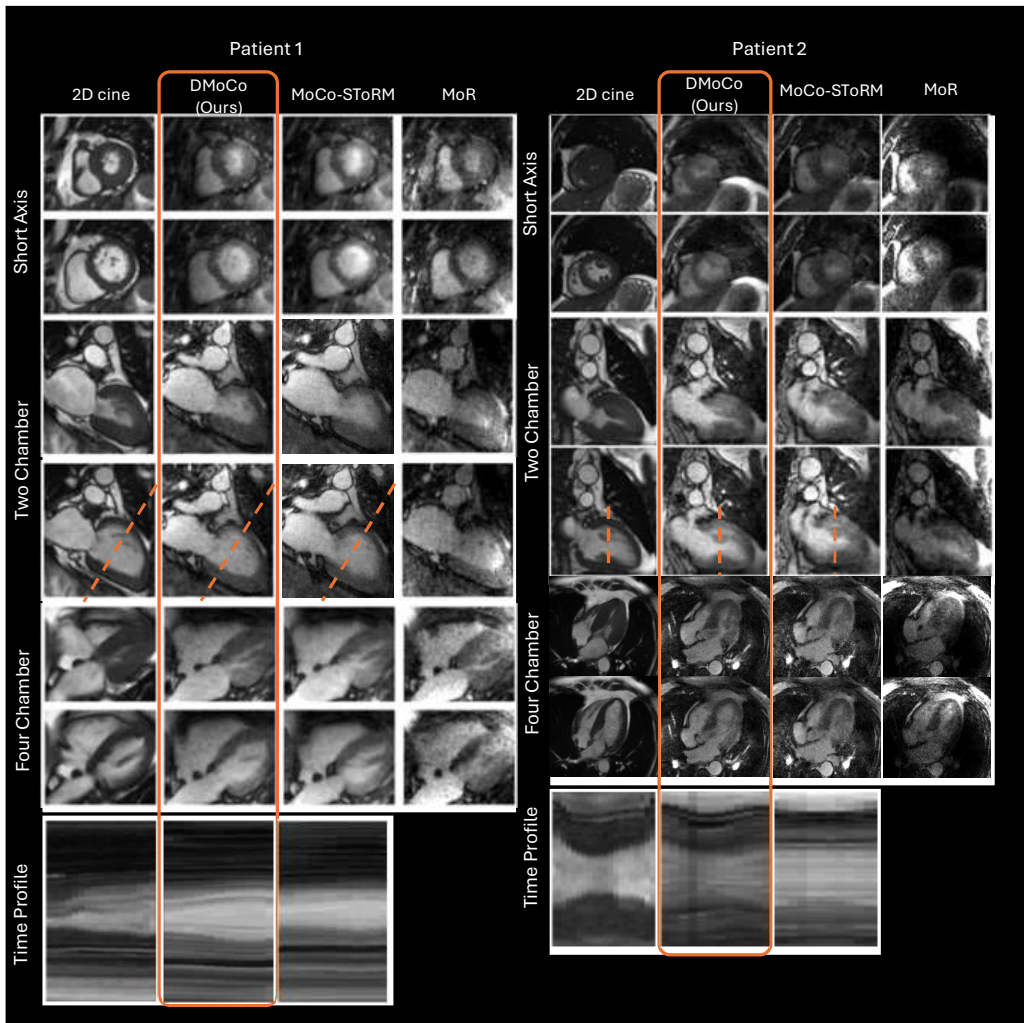


Fig. 5. In-vivo experiments: We show the reconstructions obtained using DMoCO, MoCo-SToRM, and a motion resolved (MoR) approach top. We show the reconstructed short-axis and long-axis views and compare them against 2D cine. The top row of each view indicates ventricular systole, while the bottom corresponds to diastole. The bottom row shows the time profile of the red-dotted line in the two-chambered view. The first column shows the 2D cine images, followed by our proposed method DMoCo, [34], and MoR.

function of the cardiac phases. We also observe that the images recovered using DMoCo are less blurred and more consistent with the reference compared to MoCo-SToRM. Finally, we measure the respiratory displacement from the left dome of the diaphragm to be 26.06 mm for DMoCo, 21.69 mm for MoCo-SToRM, compared to the ground truth of 27.33 mm for the XCAT phantom.

#### D. In Vivo Results

The reconstructed images using the proposed DMoCo approach, MoCo-SToRM, and a motion resolved approach from

two patients are shown in Fig. 5. The first row corresponds to short-axis reconstructions in the systole, while the second row corresponds to the diastole. We also show results in the two-chamber and four-chamber views. The first column denotes the 2D SSFP cine acquisitions. We note that the contrast of the 2D cine acquisition is superior to that of the 3D acquisition, mainly because of the inflow effects. In contrast, the saturation of the magnetization in the 3D radial acquisition translates to a lower contrast-to-noise ratio between the blood pool and the myocardium. This is consistent with the literature [20].

We note that the reconstructions with motion-resolved

(MoR) method appear more noisy than the motion-compensated (MoCo) schemes. As noted before, the motion-resolved schemes are sensitive to uneven sampling of the bins; the radial undersampling artifacts manifest as noise in the reconstructions. In contrast, motion-compensated methods combine the data from different motion states to recover the static template, which translates to reducing noise and artifacts. We do not show the temporal profiles of MR because it only has five cardiac phases. The results also show that the time profiles of the proposed model are more comparable to 2D cine, compared to MoCo-SToRM, which tends to result in more averaged time profiles.

Additionally, 3D bSSFP lacks contrast due to blood flowing into the imaging plane like 2D cine. Interestingly, we found the static template converged to ventricular systole even though the heart spends less time in systole than diastole.

## VII. DISCUSSION

The proposed DMoCo approach represents the images at the different motion phases as deformed versions of a static template. The deformation at a specific motion phase is represented as a diffeomorphism, obtained by integrating a parametric velocity field over intermediate phases as shown in (7). The parametric velocity field itself is represented using a low-rank model, while a velocity constraint is added to encourage the deformations to be path-independent. The parameters of the low-rank model and the static template are learned directly from the k-space data in a patient-specific, self-supervised fashion. The experiments on the numerical phantom show that the DMoCo model is more constrained than the MoCo-SToRM approach, which uses a low-rank representation to directly model the deformations. In particular, Fig. 2 shows that the velocity fields, which are integrated to produce the deformation fields, can be of a lower rank than the deformation fields themselves. We also see from the results in Fig. 3 that the addition of the velocity constraints further regularizes the representation, while being able to accurately model the deformations. The integration of velocity fields over the different intermediate phases to produce the deformation serves as a smoothness constraint between adjacent motion phases, translating to improved preservation of time profiles, as seen from Fig. 4; the lack of a smoothness constraint in MoCo-SToRM resulted in abrupt discontinuities in the time profiles and blurred reconstructions. This trend is also supported by the respiratory displacement (RD) which is 21.69mm for MoCo-SToRM and 26.06mm for DMoCo compared to the ground truth of 27.33mm.

The experiments on in-vivo data are in line with the phantom results. We observe that the time profiles of DMoCo are more in agreement with the 2D cine acquisitions. The proposed scheme reduced the noise and alias artifacts compared to a motion-resolved reconstruction; the averaging of the different motion phases to yield the template enables the motion compensation methods to be more resilient to undersampling and noise.

A potential benefit of the proposed scheme is its ability to provide deformation maps. Although we have not studied the

utility of these maps in estimating myocardial strain, this will be considered in the future. The focus of the present paper is to introduce the novel reconstruction algorithm and demonstrate its preliminary utility; the evaluation of the strain maps is beyond the scope of the present work.

Despite promising results, the proposed study still has some limitations that restrict data quality, which we aim to overcome in our future studies. A challenge is the low contrast-to-noise ratio (CNR) in 3D acquisitions. Unlike 2D scans that present good inflow contrast from unsaturated blood that flows into the imaging slice, the contrast in 3D acquisitions is inherently low. A possible alternative is a 3D multislab or interleaved multi-slice acquisition, which may offer improved contrast. Another challenge is that our current sequence did not employ fat suppression, resulting in strong residual streak artifacts. We will employ intermittent pulses of fat saturation as in [5] to minimize residual fat signals. Furthermore, current studies show the exciting possibility of significantly improving CNR in 3D studies by using ferumoxytol [4], which may be another option to improve CNR.

The computational complexity of the current unsupervised approach is around 3 hours to reconstruct a dataset on an A100 GPU. While this is faster than the current motion resolved approaches, we believe that it can be accelerated in the future. We will consider more efficient variable splitting strategies or improved deep learning based priors (e.g. [7]) on the template or initialization strategies, which may help manage the computational complexity.

## VIII. CONCLUSION

An unsupervised motion-compensated image reconstruction algorithm was introduced for free-breathing and ungated 3D cardiac MRI. The images at different motion phases were expressed as the deformation of a static image template, where the deformations are represented using low-rank diffeomorphic flow model. The static template and low-rank motion model parameters were learned directly from the k-space data in an unsupervised manner. The experiments show that the MoCo approach is less sensitive to undersampling of the motion phases. The more constrained motion model translated to more robust motion estimates, which offers improved performance compared to MoCo methods that directly model the deformations.

## REFERENCES

- [1] XCAT Phantom Program - CVIT - Center for Virtual Imaging Trials — cvit.duke.edu. <https://cvit.duke.edu/resource/xcat-phantom-program/>. [Accessed 11-03-2025].
- [2] Syed M. Arshad, Lee C. Potter, Chong Chen, Yingmin Liu, Preethi Chandrasekaran, Christopher Crabtree, Matthew S. Tong, Orlando P. Simonetti, Yuchi Han, and Rizwan Ahmad. Motion-robust free-running volumetric cardiovascular mri. *Magnetic Resonance in Medicine*, May 2024.
- [3] Guha Balakrishnan, Amy Zhao, Mert R. Sabuncu, John Guttag, and Adrian V. Dalca. VoxelMorph: A Learning Framework for Deformable Medical Image Registration. *IEEE Transactions on Medical Imaging*, 38(8), 2019.
- [4] Mustafa R. Bashir, Lubna Bhatti, Daniele Marin, and Rendon C. Nelson. Emerging applications for ferumoxytol as a contrast agent in mri. *Journal of Magnetic Resonance Imaging*, 41(4):884–898, June 2014.

- [5] Jessica A.M. Bastiaansen, Davide Piccini, Lorenzo Di Sopra, Christopher W. Roy, John Heerfordt, Robert R. Edelman, Ioannis Koktzoglou, Jérôme Yerly, and Matthias Stuber. Natively fat-suppressed 5d whole-heart mri with a radial free-running fast-interrupted steady-state (fiss) sequence at 1.5t and 3t. *Magnetic Resonance in Medicine*, 83(1):45–55, August 2019.
- [6] M. Faisal Beg, Michael I. Miller, Alain Trouvé, and Laurent Younes. Computing large deformation metric mappings via geodesic flows of diffeomorphisms. *International Journal of Computer Vision*, 61(2), 2005.
- [7] Jyothi Rikhab Chand and Mathews Jacob. Multi-scale energy (muse) framework for inverse problems in imaging. *IEEE Transactions on Computational Imaging*, 10:1250–1265, 2024.
- [8] Gary E. Christensen, Richard D. Rabbitt, and Michael I. Miller. Deformable templates using large deformation kinematics. *IEEE Transactions on Image Processing*, 5(10), 1996.
- [9] Simone Coppo, Davide Piccini, Gabriele Bonanno, Jérôme Chaptinel, Gabriella Vincenti, Hélène Feliciano, Ruud B. van Heeswijk, Juerg Schwiter, and Matthias Stuber. Free-running 4d whole-heart self-navigated golden angle mri: Initial results. *Magnetic Resonance in Medicine*, 74(5):1306–1316, November 2014.
- [10] Lorenzo Di Sopra, Davide Piccini, Simone Coppo, Matthias Stuber, and Jérôme Yerly. An automated approach to fully self-gated free-running cardiac and respiratory motion-resolved 5d whole-heart mri. *Magnetic Resonance in Medicine*, 82(6):2118–2132, July 2019.
- [11] Li Feng, Leon Axel, Hersh Chandarana, Kai Tobias Block, Daniel K. Sodickson, and Ricardo Otazo. Xd-grasp: Golden-angle radial mri with reconstruction of extra motion-state dimensions using compressed sensing. *Magnetic Resonance in Medicine*, 75(2):775–788, March 2015.
- [12] Li Feng, Simone Coppo, Davide Piccini, Jerome Yerly, Ruth P. Lim, Pier Giorgio Masci, Matthias Stuber, Daniel K. Sodickson, and Ricardo Otazo. 5d whole-heart sparse mri. *Magnetic Resonance in Medicine*, 79(2):826–838, May 2017.
- [13] Wenqi Huang, Hongwei Bran Li, Jiazhen Pan, Gastao Cruz, Daniel Rueckert, and Kerstin Hammernik. Neural Implicit k-Space for Binning-free Non-Cartesian Cardiac MR Imaging. *Lecture Notes in Computer Science (including subseries Lecture Notes in Artificial Intelligence and Lecture Notes in Bioinformatics)*, 13939 LNCS:548–560, 12 2022.
- [14] Joseph Kettelkamp, Ludovica Romanin, Davide Piccini, Sarv Priya, and Mathews Jacob. *Motion Compensated Unsupervised Deep Learning for 5D MRI*, page 419–427. Springer Nature Switzerland, 2023.
- [15] Thomas Küstner, Aurélien Bustin, Olivier Jaubert, Reza Hajhosseiny, Pier Giorgio Masci, Radhouene Neji, René Botnar, and Claudia Prieto. Fully self-gated free-running 3d cartesian cardiac cine with isotropic whole-heart coverage in less than 2 min. *NMR in Biomedicine*, 34(1), September 2020.
- [16] Zengyi Li, Yubei Chen, and Friedrich T. Sommer. Learning Energy-Based Models in High-Dimensional Spaces with Multiscale Denoising-Score Matching. *Entropy* 2023, Vol. 25, Page 1367, 25(10):1367, 9 2023.
- [17] Jing Liu, Pascal Spincemaille, Noel C. F. Codella, Thanh D. Nguyen, Martin R. Prince, and Yi Wang. Respiratory and cardiac self-gated free-breathing cardiac cine imaging with multiecho 3d hybrid radial ssfp acquisition. *Magnetic Resonance in Medicine*, 63(5):1230–1237, April 2010.
- [18] Mehdi H. Moghari, Ashita Barthur, Maria E. Amaral, Tal Geva, and Andrew J. Powell. Free-breathing whole-heart 3d cine magnetic resonance imaging with prospective respiratory motion compensation. *Magnetic Resonance in Medicine*, 80(1):181–189, December 2017.
- [19] Camila Munoz, Haikun Qi, Gastao Cruz, Thomas Küstner, René M. Botnar, and Claudia Prieto. Self-supervised learning-based diffeomorphic non-rigid motion estimation for fast motion-compensated coronary MR angiography. *Magnetic resonance imaging*, 85:10–18, 1 2022.
- [20] Reza Nezafat, Daniel Herzka, Christian Stehning, Dana C. Peters, Kay Nehrke, and Warren J. Manning. Inflow quantification in three-dimensional cardiovascular mr imaging. *Journal of Magnetic Resonance Imaging*, 28(5):1273–1279, October 2008.
- [21] Freddy Odille, Anne Menini, Jean Marie Escanyé, Pierre André Vuissoz, Pierre Yves Marie, Marine Beaumont, and Jacques Felblinger. Joint reconstruction of multiple images and motion in MRI: Application to free-breathing myocardial quantification. *IEEE Transactions on Medical Imaging*, 35(1):197–207, 1 2016.
- [22] Jiazhen Pan, Manal Hamdi, Wenqi Huang, Kerstin Hammernik, Thomas Kuestner, and Daniel Rueckert. Unrolled and rapid motion-compensated reconstruction for cardiac CINE MRI. *Medical Image Analysis*, 91:103017, 1 2024.
- [23] Jianing Pang, Behzad Sharif, Zhaoyang Fan, Xiaoming Bi, Reza Arsanjani, Daniel S. Berman, and Debiao Li. Ecg and navigator-free four-dimensional whole-heart coronary mra for simultaneous visualization of cardiac anatomy and function. *Magnetic Resonance in Medicine*, 72(5):1208–1217, September 2014.
- [24] Andrew Phair, Anastasia Fotaki, Lina Felsner, Thomas J. Fletcher, Haikun Qi, René M. Botnar, and Claudia Prieto. A motion-corrected deep-learning reconstruction framework for accelerating whole-heart magnetic resonance imaging in patients with congenital heart disease. *Journal of Cardiovascular Magnetic Resonance*, 26(1):101039, 2024.
- [25] Davide Piccini, Arne Littmann, Sonia NIELLES-Vallespin, and Michael O. Zenge. Spiral phyllotaxis: The natural way to construct a 3d radial trajectory in mri. *Magnetic Resonance in Medicine*, 66(4):1049–1056, April 2011.
- [26] Sebastian Rosenzweig, Nick Scholand, H. Christian M. Holme, and Martin Uecker. Cardiac and respiratory self-gating in radial mri using an adapted singular spectrum analysis (ssa-fary). *IEEE Transactions on Medical Imaging*, 39(10):3029–3041, October 2020.
- [27] Christopher W. Roy, Bastien Milani, Jérôme Yerly, Salim Si-Mohamed, Ludovica Romanin, Aurélien Bustin, Estelle Tenisch, Tobias Rutz, Milan Prsa, and Matthias Stuber. Intra-bin correction and inter-bin compensation of respiratory motion in free-running five-dimensional whole-heart magnetic resonance imaging. *Journal of Cardiovascular Magnetic Resonance*, 26(1):101037, 2024.
- [28] Veronika Spieker, Wenqi Huang, Hannah Eichhorn, Jonathan Stelter, Kilian Weiss, Veronika A. Zimmer, Rickmer F. Braren, Dimitrios C. Karampinos, Kerstin Hammernik, and Julia A. Schnabel. ICoNIK: Generating Respiratory-Resolved Abdominal MR Reconstructions Using Neural Implicit Representations in k-Space. 8 2023.
- [29] M. Usman, B. Ruijsink, M.S. Nazir, G. Cruz, and C. Prieto. Free breathing whole-heart 3d cine mri with self-gated cartesian trajectory. *Magnetic Resonance Imaging*, 38:129–137, May 2017.
- [30] Jaejun Yoo, Kyong Hwan Jin, Harshit Gupta, Jerome Yerly, Matthias Stuber, and Michael Unser. Time-Dependent Deep Image Prior for Dynamic MRI. *IEEE Transactions on Medical Imaging*, 40(12):3337–3348, 12 2021.
- [31] Xucheng Zhu, Marilynn Chan, Michael Lustig, Kevin M. Johnson, and Peder E. Z. Larson. Iterative motion-compensation reconstruction ultrashort te (imoco ute) for high-resolution free-breathing pulmonary mri. *Magnetic Resonance in Medicine*, 83(4):1208–1221, September 2019.
- [32] Qing Zou, Abdul Haseeb Ahmed, Prashant Nagpal, Stanley Kruger, and Mathews Jacob. Dynamic imaging using a deep generative STORM (Gen-STORM) model. *IEEE transactions on medical imaging*, 40(11):3102, 11 2021.
- [33] Qing Zou, Abdul Haseeb Ahmed, Prashant Nagpal, Sarv Priya, Rolf F. Schulte, and Mathews Jacob. Variational Manifold Learning From Incomplete Data: Application to Multislice Dynamic MRI. *IEEE transactions on medical imaging*, 41(12):3552–3561, 12 2022.
- [34] Qing Zou, Luis A. Torres, Sean B. Fain, Nara S. Higano, Alister J. Bates, and Mathews Jacob. Dynamic imaging using motion-compensated smoothness regularization on manifolds (MoCo-STORM). *Physics in Medicine & Biology*, 67(14):144001, 7 2022.